OPEN

NPG Asia Materials (2017) 9, e407; doi:10.1038/am.2017.114
www.nature.com/am

ORIGINAL ARTICLE

Bimetallic AuRh nanodendrites consisting of Au icosahedron cores and atomically ultrathin Rh nanoplate shells: synthesis and light-enhanced catalytic activity

Yongqiang Kang[1], Qi Xue[1], Ruili Peng, Pujun Jin, Jinghui Zeng, Jiaxing Jiang and Yu Chen

Precise control of the morphology, composition and structure of metal nanostructures not only effectively improves their catalytic activity and durability but also enhances their range of applications. In this work, bimetallic Au@Rh core–shell nanodendrites are synthesized by a facile one-pot hydrothermal method. Physical characterizations show that the dendritic Rh consists of two-dimensional (2D) ultrathin Rh nanoplates with a thickness of approximately 1.2 nm. For the first time, Au@Rh core–shell nanostructures are used as a catalyst for the hydrogen generation reaction from aqueous hydrazine solution ($N_2H_4 = N_2+2H_2$, HGR-N_2H_4). Bimetallic Au@Rh core–shell nanodendrites exhibit improved catalytic activity and durability for the HGR-N_2H_4 compared with commercial Rh nanocrystals, which can be attributed to the atomically ultrathin structure of 2D Rh nanoplates and the interconnected structure of nanodendrites, respectively. Under light irradiation, bimetallic Au@Rh core–shell nanodendrites show light-enhanced catalytic activity for the HGR-N_2H_4, originating from the distinctive localized surface plasmon resonance of Au icosahedron cores.

NPG Asia Materials (2017) **9,** e407; doi:10.1038/am.2017.114; published online 14 July 2017

INTRODUCTION

Bimetallic noble metal nanostructures have been used in a variety of important industrial applications, especially in heterogeneous catalysis.[1–6] The physical and chemical properties of bimetallic noble metal nanostructures not only depend on their chemical compositions but also are related to their morphologies.[4–9] In general, bimetallic nanostructures display remarkably improved catalytic activity and selectivity compared with the corresponding monometallic nanocrystals due to the strong ensemble and ligand effects between the different components (that is, geometrical and electronic effects).[4–7,9] Meanwhile, noble metal nanodendrites with branched arms are attracting tremendous attention for the catalytic applications due to their large surface area, unusual interconnected and porous structure and abundance of low-coordination atoms at steps and corners.[10,11] Consequently, bimetallic noble metal nanodendrites have a broad variety of applications, ranging from organic synthesis to energy conversion.[12,13]

Among various bimetallic nanostructures, Au-based core–shell-type noble metal nanostructures have been widely employed in various important heterogeneous catalytic reactions, especially in light-enhanced catalytic reactions, originating from the high mass activity of noble metal shells and the distinctive localized surface plasmon resonance (LSPR) of Au nanocrystal cores.[14–17] In most bimetallic core–shell nanodendrites, the metal shells consist of spherical nanocrystals.[5,18,19] Recently, the atomically thick noble metal nanoplates, an emerging star nanomaterial for the catalysis, have attracted more attention compared with the traditional zero-dimensional noble metal nanocrystals, owing to the extremely high meal atom utilization and superior catalytic activity.[20–26] Obviously, bimetallic core–shell nanodendrites with atomically ultrathin nanoplate shells are expected to possess greatly improved catalytic activity. No such bimetallic core–shell nanodendrites have been reported to date.

Rh nanostructures are widely applied in catalytic reactions such as hydrogen generation,[27] electrocatalytic oxidation,[28] hydrogenation[29] and hydroformylation.[30] In particular, in the field of hydrogen generation, Rh nanostructures have been proved to be highly efficient catalysts for the catalytic hydrolysis of chemical hydrides (such as $N_2H_4{\cdot}H_2O$[27] and NH_3BH_3[31]). Previous studies have reported that Au@Pt and Au@Pd core–shell nanostructures showed light-enhanced catalytic activity for hydrogen generation from water–methanol[32] and formic acid,[17] respectively. Encouraged by these impressive results, we

Key Laboratory of Macromolecular Science of Shaanxi Province, Key Laboratory of Applied Surface and Colloid Chemistry (MOE), Shaanxi Engineering Lab for Advanced Energy Technology, School of Materials Science and Engineering, Shaanxi Normal University, Xi'an, People's Republic of China
[1]These authors contributed equally to this work.
Correspondence: Associate Professor P Jin or Professor Y Chen, Key Laboratory of Macromolecular Science of Shaanxi Province, Key Laboratory of Applied Surface and Colloid Chemistry (MOE), Shaanxi Engineering Lab for Advanced Energy Technology, School of Materials Science and Engineering, Shaanxi Normal University, No. 620, West Chang'an Avenue, Chang'an District, Xi'an 710119, People's Republic of China.
E-mail: jinpj@snnu.edu.cn or ndchenyu@gmail.com
Received 3 February 2017; revised 12 April 2017; accepted 3 May 2017

try to synthesize bimetallic Au@Rh core–shell nanostructures and explore their application in the field of hydrogen generation under visible light irradiation conditions. So far, bimetallic Au@Rh core–shell nanostructures are rarely synthesized,[19,33,34] which may be ascribed to the unfavorable thermodynamic equilibrium due to the large lattice mismatch (7%, Au 0.408 nm versus Rh 0.380 nm)[34,35] and large surface energy variance (43%, Au 1.6 $J\,m^{-2}$ versus Rh 2.8 $J\,m^{-2}$).[28,35,36] In this work, we demonstrated that bimetallic Au@Rh core–shell nanodendrites with a well-defined octahedral Au core and a dendritic Rh shell could be easily achieved by a facile one-pot hydrothermal method, using polyallylamine hydrochloride (Supplementary Scheme S1A) as a surfactant and diethylene glycol (Supplementary Scheme S1B) as a reductant. The physical characterization indicated that the dendritic Rh shells were composed of the atomically thick two-dimensional (2D) ultrathin Rh nanoplates. Owing to the ultrathin structure of 2D Rh nanoplates and the LSPR effect of Au icosahedron cores, bimetallic Au@Rh core–shell nanodendrites exhibited remarkably improved catalytic activity for the hydrogen generation reaction from aqueous hydrazine solution ($N_2H_4 = N_2+2H_2$, HGR-N_2H_4) under visible light irradiation conditions.

EXPERIMENTAL PROCEDURES

Reagents and chemicals

Polyallylamine hydrochloride with a weight-average molar mass of 20 000 was supplied from Nitto Boseki Co., Ltd. (Tokyo, Japan). Diethylene glycol was purchased from Sigma Aldrich (Milwaukee, WI, USA). Rhodium(III) chloride hydrate ($RhCl_3{\cdot}3H_2O$), hydrogen tetrachloroaurate(III) tetrahydrate ($HAuCl_4{\cdot}4H_2O$) and hydrazine monohydrate ($N_2H_4{\cdot}H_2O$, 85%) were obtained from the Sinopharm Chemical Reagent Co., Ltd (Shanghai, China). Other chemicals used in this work were of analytical reagent grade.

Synthesis of bimetallic Au@Rh core–shell nanodendrites

In a typical synthesis, $RhCl_3$ aqueous solution (6.0 ml, 0.01 M), polyallylamine hydrochloride aqueous solution (1.6 ml, 0.5 M), diethylene glycol solution (4.0 ml) and $HAuCl_4$ solution (3 ml, 0.01 M) were mixed and stirred for 10 min. Then the homogeneous mixture solution was transferred into a Teflon-lined high-pressure vessel and heated at 180 °C for 6 h. Finally, the obtained bimetallic Au@Rh core–shell nanodendrites were separated by centrifugation and washed with acetic acid for 10 h.[37] For comparison, monometallic Au nanocrystals were prepared in the absence of $HAuCl_4$ and monometallic Rh nanodendrites were synthesized in the absence of $RhCl_3$.

Materials characterizations

UV–visible (UV–vis) absorption spectroscopy was performed using a Shimadzu UV-3600U spectrophotometer (Shimadzu Corporation, Kyoto, Japan). Transmission electron microscopy (TEM) images, high-resolution TEM images, high-angle annular dark field scanning TEM images and energy-dispersive X-ray (EDX) spectra were obtained using a TECNAI G2 F20 transmission electron microscope (FEI Company, Hillsboro, OR, USA). Scanning electron microscopic images were obtained using a Hitachi SU-8020 emission scanning electron microscope (Hitachi High-Technologies Corporation, Tokyo, Japan). X-ray diffraction (XRD) measurements were carried out using a DX-2700 diffractometer (Dandong Haoyuan Instrument Co. Ltd, Dandong, China) with Cu-Kα radiation. X-ray photoelectron spectroscopic (XPS) measurements were performed using an AXIS ULTRA spectrometer (Shimadzu/Kratos Analytical, Hadano, Kanagawa, Japan) with Al Kα radiation as the excitation source, and the binding energy scale was calibrated with respect to adventitious carbon (C1s, 284.6 eV). Atomic force microscopic analysis was performed in the tapping mode in air using a Dimension Icon system (Bruker Corporation, Santa Barbara, CA, USA). The inductively coupled plasma atomic emission spectrometric measurements were performed using an ICP-Prodigy7 analyzer (Teledyne Leeman Labs, Hudson, NH, USA).

Hydrogen generation reaction from aqueous hydrazine solution ($N_2H_4 = N_2+2H_2$, HGR-N_2H_4)

The experimental setup for the HGR-N_2H_4 was similar to that described in a previous report.[38] The solution temperature was set to 30 °C using cycling water. Typically, the NaOH solution (4 ml, 0.5 M) containing an amount of catalyst was placed in a three-necked round-bottom flask. Then the $N_2H_4{\cdot}H_2O$ solution (0.02 ml) was injected into the sealed flask under vigorous stirring. The catalyst/$N_2H_4{\cdot}H_2O$ molar ratio was fixed at 1:10 for the catalytic reaction. The released gas was collected by a gas burette filled with water connected to the reaction flask. Before the volume was measured, the gas released from the flask was passed through a trap containing an H_2SO_4 solution (1.0 M). To determine the reaction activation energy (E_a), cycling water was used to modulate the temperature of the reaction system. For the light-enhanced catalytic experiment, the reaction solution was exposed to light irradiation from a Xenon lamp (power density of 0.33 W cm^2) under vigorous stirring.

The turnover frequency (TOF) value was calculated as[39]:

$$\mathrm{TOF}_{\mathrm{initial}} = \frac{P_{\mathrm{atm}} V_{\mathrm{H_2+N_2}}/\mathrm{R}T}{3n_{\mathrm{metal}}t} \quad (1)$$

where $\mathrm{TOF}_{\mathrm{initial}}$ is the initial turnover frequency, P_{atm} is the atmospheric pressure, $V_{\mathrm{H2+N2}}$ is the volume of the generated gas (H_2+N_2) when the conversion reached 50%, R is the universal gas constant, T is the temperature (298 K), n_{metal} is the mole number of metal catalyst and t is the reaction time when the conversion reached 50%.

The reaction E_a was calculated by the Arrhenius equation as[40]:

$$\ln\mathrm{TOF} = \ln \mathrm{A} - E_a/\mathrm{R}T \quad (2)$$

where A is the reaction constant.

For the durability test, the catalytic reaction was repeated seven times by adding another equivalent of $N_2H_4{\cdot}H_2O$ into the reaction vessel after the completion of the previous cycle.

RESULTS AND DISCUSSION

Characterization of bimetallic Au@Rh core–shell nanodendrites

Bimetallic Au@Rh core–shell nanodendrites were easily achieved by heating the mixture solution of $RhCl_3$, $HAuCl_4$, polyallylamine hydrochloride and diethylene glycol (see Experimental procedures for details). The morphology, size and chemical composition of the products were first investigated by scanning electron microscopy and EDX. The scanning electron microscopic image clearly reveals that the products are uniform spherical nanocrystals with a rough surface (Figure 1a). Their mean particle diameter is approximately 90 nm (Supplementary Figure S1). EDX measurements indicate that the products mainly contain Au and Rh elements (Figure 1b). The Au/Rh atomic ratio is quantitatively determined by inductively coupled plasma atomic emission spectrometric analysis to be approximately 63:37, which is close to the theoretical stoichiometric ratio. The chemical states of Au and Rh species were identified by XPS. The Au 4f and Rh 3d XPS spectra show that the metallic Au^0 and Rh^0 are the predominant species (Figure 1c), indicating that both $RhCl_3$ and $HAuCl_4$ precursors are reduced successfully. However, XPS analysis shows that the Au/Rh atomic ratio is 8.4:91.6 (Supplementary Figure S2), which is much lower than the value obtained by EDX analysis (Au/Rh = 66:34). It is well known that XPS is a highly sensitive surface analysis technique with an analysis depth of approximately 1–5 nm, whereas EDX is a bulk analysis technique with an analysis depth of approximately 1000–2000 nm. The discrepancy between the XPS and EDX results suggests that the products are not a uniform AuRh alloy. Indeed, the XRD pattern shows two distinct sets of diffraction peaks, which can be assigned to the diffraction patterns of Au and Rh crystals, respectively (Figure 1d). Thus the XRD pattern further confirms that no alloy phase exists in the products.

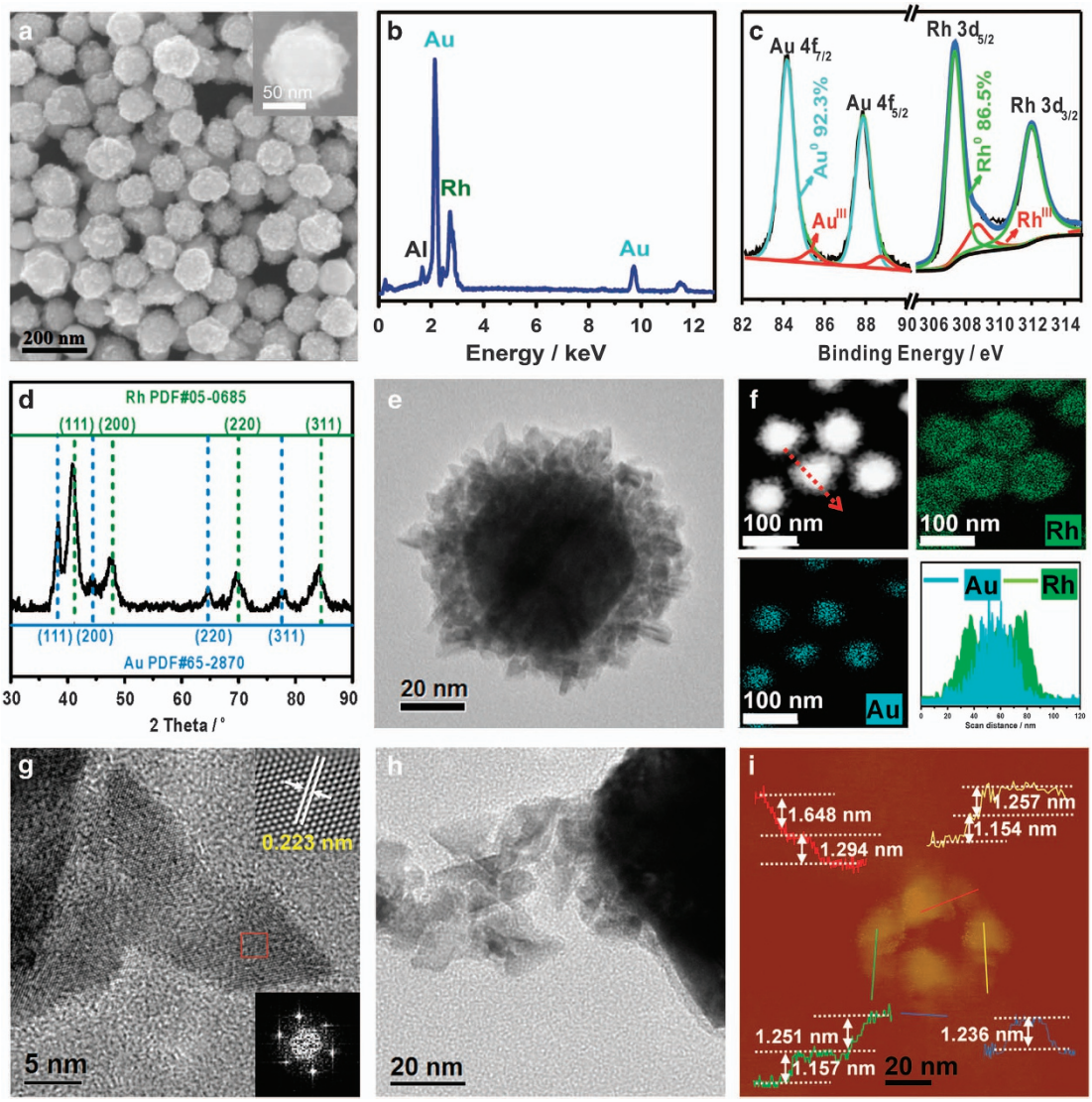

Figure 1 (**a**) Scanning electron microscopic (SEM) image, inset: magnified SEM image, (**b**) EDX spectrum, (**c**) Au 4f and Rh 3d XPS spectra, (**d**) XRD pattern and (**e**) High-resolution TEM (HRTEM) image of bimetallic Au@Rh core–shell nanodendrites. (**f**) high-angle annular dark field scanning TEM image, EDX mapping pattern and line scanning pattern of bimetallic Au@Rh core–shell nanodendrites. (**g**) Magnified HRTEM image of the dendritic Rh shells. Top inset: further magnified HRTEM image; bottom inset: corresponding Fast-Fourier transform (FFT) pattern. (**h**) HRTEM and (**i**) atomic force microscopic images of Rh nanoplates obtained by the strong ultrasonic treatment.

The morphology and structure of the products were further investigated by high-resolution TEM. The products show obvious dendritic morphology (Figure 1e), and the average particle size is ca. 87 nm (Supplementary Figure S3), in agreement with the scanning electron microscopic result. The strong luminance contrast between the center and the edge indicates that the products have a core–shell structure (Figure 1e). EDX mapping and line scanning patterns reveal that the nanodendrites are composed of an Au core and an Rh shell (Figure 1f). Here the size of the Au core is approximately 55 nm, whereas the thickness of the Rh shell is approximately 16 nm. The magnified high-resolution TEM image shows that the dendritic Rh shells are composed of Rh nanoplates (Figure 1g). The lattice spacing between the two lattice fringes is approximately 0.223 nm (top inset in Figure 1g), corresponding to Rh(111) facets. The fast-Fourier transform pattern clearly shows one diffraction pattern with six-fold rotational symmetry (bottom inset in Figure 1g), confirming Rh(111) facets. After strong ultrasonic treatment, few Rh nanoplates are observed (Figure 1h), further confirming that the dendritic Rh shells are composed of Rh nanoplates. Atomic force microscopic measurement show that the Rh nanoplates are only approximately 1.2 nm thick (Figure 1i), corresponding to approximately four atomic layers.

Formation mechanism of bimetallic Au@Rh core–shell nanodendrites

To understand the formation mechanism of bimetallic Au@Rh core–shell nanodendrites, the reaction process was first monitored by UV–vis spectroscopy (Figure 2a). The reduction potential of Au^{III} ($\varphi HAuCl_4/Au$, +0.99 V versus the standard hydrogen electrode)[41] is higher than that of Rh^{III} ($\varphi RhCl_3/Rh$, +0.76 V versus the standard hydrogen electrode).[42] Thus the $HAuCl_4$ precursor may be reduced preferentially to generate Au nanocrystals during the synthesis that will subsequently act as the cores for the growth of the Rh shells.

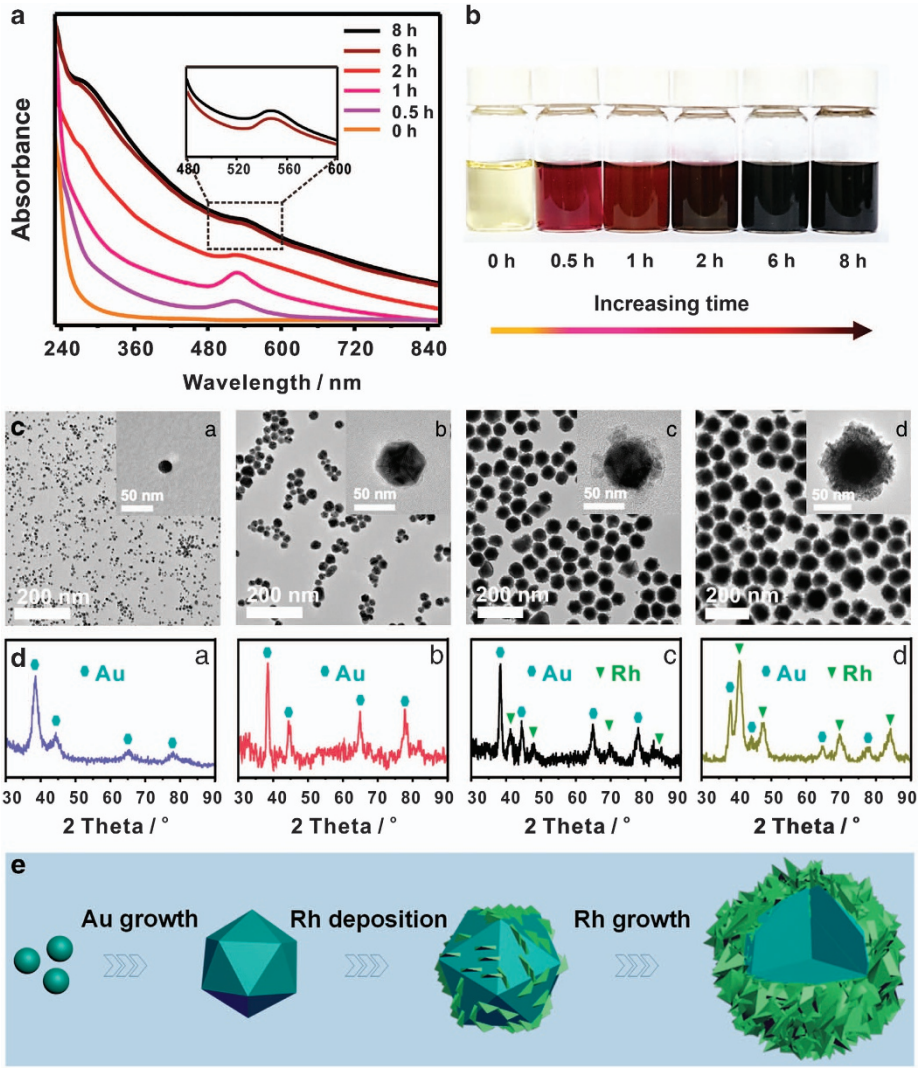

Figure 2 (**a**) UV–vis spectra, inset: enlarged UV spectrum and (**b**) photographs of the actual reaction system at different times. (**c**) TEM images and (**d**) corresponding XRD patterns of the reaction intermediates at (a) 0.5, (b) 1, (c) 2 and (d) 6 h, respectively. (**e**) Schematic illustration of the formation process of bimetallic Au@Rh core–shell nanodendrites.

As expected, no characteristic absorption peak of Au nanocrystals is observed at the initial reaction time (that is, 0 h). At 0.5 h, the UV–vis spectrum exhibits a strong visible light absorption at 520 nm, indicating the formation of Au nanocrystals.[43] When the reaction time increased to 1 h, the absorption peak at 520 nm increased accordingly, indicating the growth of Au nanocrystals. At 2 h, the absorption peak of Au became weaker as a result of the deposition of Rh on the surfaces of the Au nanocrystals.[19,44] At 6 h, the absorption peak of the Au nanocrystals weakened further, which is ascribed to the continuous growth of Rh shells on the Au nanocrystals. Upon further increasing the reaction time to 8 h, UV–vis curve remains almost constant, indicating the complete reduction of the $RhCl_3$ precursor within 6 h. However, the absorption peak of Au still appeared in the enlarged spectrum (inset in Figure 2a). The photographs of the actual system show color change from yellow to red to black (Figure 2b), confirming the generation of Au nanocrystal cores and the subsequently continuous deposition of Rh on the preformed Au nanocrystals, in agreement with UV–vis measurements. To visualize the growth process of bimetallic Au@Rh core–shell nanodendrites, the intermediates at different reaction times were collected and characterized by TEM and XRD. At 0.5 h, the ultrafine Au nanocrystals are generated (Figure 2c(a)), and these Au nanocrystals have a spherical morphology (Supplementary Figure S4). For a reaction time of 1 h, the ultrafine Au nanocrystals have grown into Au icosahedra (Figure 2c(b) and Supplementary Figure S5). At 2 h, some Rh nanocrystals aggregate around the preformed Au icosahedra (Figure 2c(c)). At 6 h, the complete bimetallic Au@Rh core–shell nanodendrites are observed (Figure 2c(d)). A series of corresponding XRD patterns shows that the Au diffraction peak intensity of the intermediates first increases and then decreases with reaction time, and the Rh diffraction peak intensity of the intermediates increases with reaction time (Figure 2d). Thus TEM and XRD results clearly indicate that the formation process of bimetallic Au@Rh core–shell nanodendrites can be easily divided into four steps, from the appearance of Au seeds to the appearance of well-defined Au@Rh core–shell structures (Figure 2e).

Effects of experimental parameters

To understand the function of diethylene glycol and polyallylamine hydrochloride during the synthesis, a set of control experiments were

performed. In the absence of diethylene glycol, only irregular Au nanocrystals are obtained at 1 h (Supplementary Figure S6), indicating that diethylene glycol is critical for the formation of Au icosahedra. In the absence of polyallylamine hydrochloride, the obvious phase separation is observed and nanocrystals exhibit self-aggregation (Supplementary Figures S7A and B), indicating that polyallylamine hydrochloride effectively acts as a capping agent and a linker agent for the deposition of Rh on the preformed Au nanocrystals during the synthesis of bimetallic Au@Rh core–shell nanodendrites. Meanwhile, in the absence of polyallylamine hydrochloride, spherical Rh nanocrystals anchor on Au nanocrystals surface instead of Rh nanoplates (Supplementary Figure S7C), indicating that polyallylamine hydrochloride has an important role for the formation of Rh nanoplates due to its strong adsorption on Rh(111) facets.[31,45] In fact, the monometallic Rh nanodendrites with ultrathin Rh nanoplate branches can easily be achieved in the absence of $HAuCl_4$ (Supplementary Figure S8), confirming that the presence of polyallylamine hydrochloride facilitates the formation of 2D ultrathin Rh nanoplates. It is worth noting that the Rh shell thickness can be easily adjusted from 7 to 32 nm by changing the amount of $RhCl_3$ (Figure 3), demonstrating a size-adjustable synthesis. When the amount of $HAuCl_4$ is decreased, the TEM image shows the presence of many monometallic Rh nanodendrites (see circle in Supplementary Figure S9), indicating that the size of Au cores also has a vital role for the formation of bimetallic Au@Rh core–shell nanodendrites.

Light-enhanced catalytic activity for the HGR-N_2H_4

Hydrogen, a clean and green energy source, has been considered as a highly promising future energy source that can effectively eliminate the environmental pollution and the greenhouse effect.[40,46] Recently, the HGR-N_2H_4 has attracted tremendous attention due to the facile storage and transportation, low cost and high hydrogen density (8 wt.%) of $N_2H_4{\cdot}H_2O$.[27,47,48] The catalytic performance of bimetallic Au@Rh core–shell nanodendrites for the HGR-N_2H_4 was first examined and compared with those of commercial Rh black and monometallic Rh nanodendrites under the same experimental conditions in the absence of light irradiation. Hydrogen generation profiles show that the hydrogen generation rate at bimetallic Au@Rh core–shell nanodendrites is much higher than that at the commercial Rh black (Figure 4a). The HGR-N_2H_4 TOF value ($8.9\,h^{-1}$) at bimetallic Au@Rh core–shell nanodendrites is 11.1 times larger than that ($0.8\,h^{-1}$) of commercial Rh black (inset in Figure 4a). Meanwhile, the TOF value is also higher than the values for the recently reported Rh-based alloy catalysts, such as $Rh_{10}Ni_{90}$ nanoparticles ($3.3\,h^{-1}$),[49] Rh_4Ni nanoparticles ($4.8\,h^{-1}$),[48] RhCu nanoframes ($5.6\,h^{-1}$)[50] and Rh_2Ni nanocubes/C ($7.1\,h^{-1}$).[51] To understand the excellent catalytic performance of bimetallic Au@Rh core–shell nanodendrites, the catalytic performance of monometallic Rh nanodendrites for the HGR-N_2H_4 was also investigated. As observed, the hydrogen generation rate and TOF of HGR-N_2H_4 at monometallic Rh nanodendrites are much larger than those at commercial Rh black (Figure 4a and inset), indicating that the ultrathin structure of Rh nanoplates contributes to the drastic activity enhancement.

According to thermodynamics theory, the catalytic activity is closely related to the reaction activation energy (E_a). A smaller E_a value generally results in a higher catalytic activity. To obtain the E_a of the HGR-N_2H_4 at bimetallic Au@Rh core–shell nanodendrites, the catalytic reactions were performed at different temperatures. As observed, the hydrogen generation rate increases gradually with temperature (Figure 4b). According to the Arrhenius plot (inset in Figure 4b), the E_a value of the HGR-N_2H_4 at bimetallic Au@Rh core–shell nanodendrites is determined to be $42.5\,kJ\,mol^{-1}$, smaller than that at commercial Rh black ($59.2\,kJ\,mol^{-1}$, Supplementary Figure S10). The previous excellent studies have demonstrated that the atoms at defect sites with low-coordination numbers are super active for the various catalytic reactions.[22,23,25] Compared with bulk metal nanoparticles, the atomically thick ultrathin nanoplates maximize the number of coordinately unsaturated active sites in the edges and exposed faces (Supplementary Scheme S2) that have an essential role in catalytic reactions.[22,25,52,53] The atomic force microscopic image indicates that the thickness of the 2D Rh nanoplate is only approximately 1.2 nm (Figure 1i), and the nanoplate contains only approximately four atomic layers. As an intrinsic property of ultrathin nanoplates, Au@Rh core–shell nanodendrites contain numerous Rh atoms at defect sites with low-coordination numbers because nearly half of the Rh atoms are present on the surface of the Rh nanoplates with four atomic layers. Obviously, the abundant defective Rh atoms in bimetallic Au@Rh core–shell nanodendrites contribute to the low E_a value, resulting in high reactivity for the HGR-N_2H_4.

The most striking feature of bimetallic Au@Rh core–shell nanodendrites is the LSPR property of the Au nanocrystal cores. Previous studies have demonstrated that the LSPR property of bimetallic core–shell nanostructures can significantly facilitate their catalytic activity for many important reactions, such as hydrogen production from water splitting,[14,15,54] dehydrogenation of formic

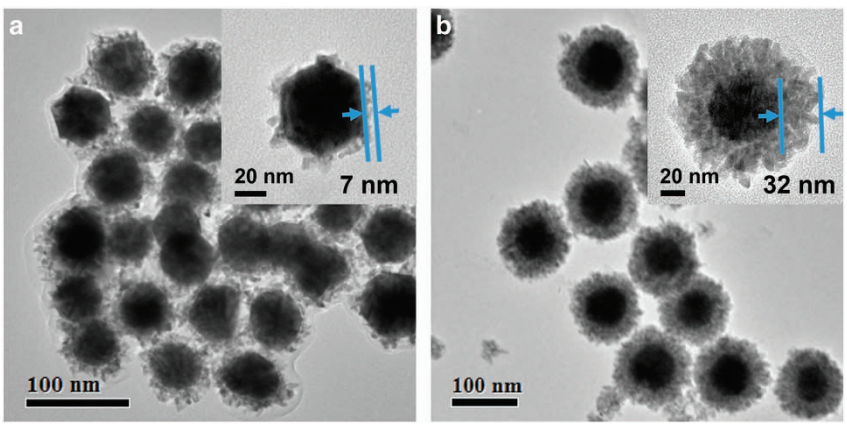

Figure 3 TEM images of bimetallic Au@Rh core–shell nanodendrites obtained by changing the molar ratio of $HAuCl_4/RhCl_3$ to (**a**) 10:1 and (**b**) 1:1.

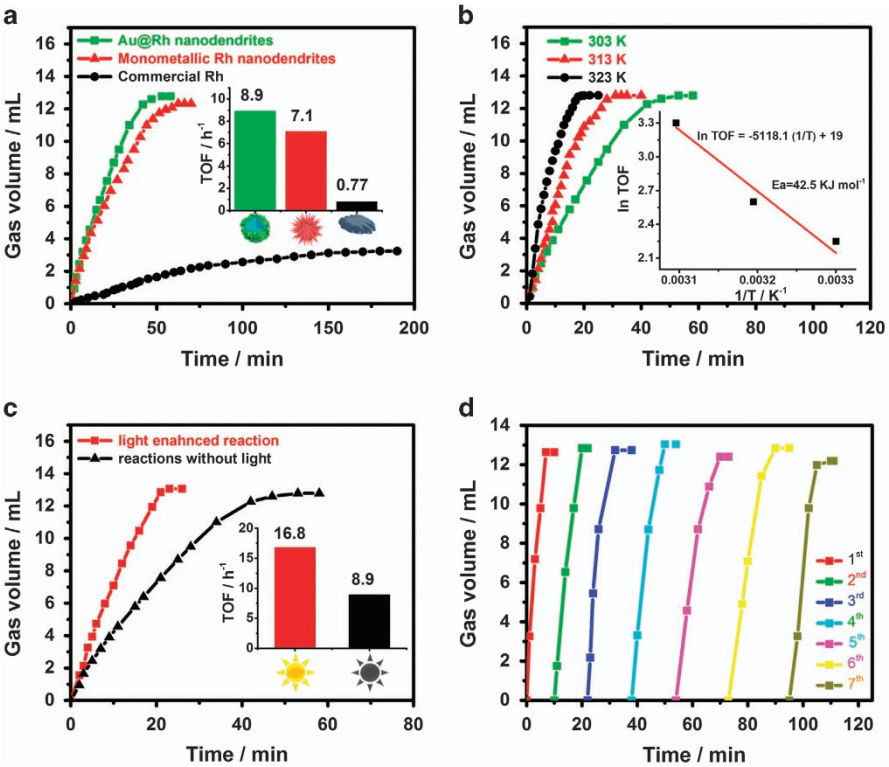

Figure 4 (**a**) Volume of the generated gas (H_2+N_2) versus time for the HGR-N_2H_4 at bimetallic Au@Rh core–shell nanodendrites, commercial Rh black and monometallic Rh nanodendrites under dark conditions. Inset: TOF values of the HGR-N_2H_4 at bimetallic Au@Rh core–shell nanodendrites, commercial Rh black and monometallic Rh nanodendrites. (**b**) Volume of the generated gas (H_2+N_2) versus time for the HGR-N_2H_4 at bimetallic Au@Rh core–shell nanodendrites at 30, 40 and 50 °C under dark conditions. Inset: Plot of ln TOF versus 1/*T* at different temperatures. (**c**) Volume of the generated gas (H_2+N_2) versus time for the HGR-N_2H_4 at bimetallic Au@Rh core–shell nanodendrites at 30 °C with and without light irradiation. (**d**) Durability test of bimetallic Au@Rh core–shell nanodendrites for the HGR-N_2H_4 with light irradiation at 30 °C.

acid[17] and a Suzuki coupling reaction.[55] The unique heterostructure and LSPR optical property of bimetallic Au@Rh core–shell nanodendrites offer the possibility of light-enhanced catalytic applications. Thus the catalytic activity of bimetallic Au@Rh core–shell nanodendrites for the HGR-N_2H_4 was investigated under dark and light irradiation conditions. Under light irradiation, the hydrogen evolution rate at bimetallic Au@Rh core–shell nanodendrites is obviously higher than that under the dark conditions (Figure 4c). It must be emphasized that monometallic Au nanocrystals show no catalytic activity for the HGR-N_2H_4 under light irradiation conditions (Supplementary Figure S11). Meanwhile, it is observed that light irradiation does not affect the catalytic performance of the monometallic Rh nanodendrites for the HGR-N_2H_4 (Supplementary Figure S12). This indicates that the Au nanocrystal cores in bimetallic Au@Rh core–shell nanodendrites have an important role for the light-enhanced catalytic activity. When Au based core–shell nanostructures are exposed to light, the electron transfer of the Au core to the metal shell generally results in the charge enrichment on the metal shell.[15–17] Previous investigations have demonstrated that the electronic properties of the metal surface have a crucial role for the HGR-N_2H_4 because N-N and N-H bond cleavage is closely related to the electronic structure of metal atoms.[27,56] For the Au@Rh core–shell nanodendrites under light irradiation conditions, the charge-enriched Rh shells effectively weaken the N-H bond and reduce the activation barrier energy,[57,58] resulting in light-enhanced catalytic activity. The corresponding TOF value ($16.8\,h^{-1}$) under the light irradiation condition is 1.9 times larger than that ($8.9\,h^{-1}$) under the dark conditions (inset in Figure 4c). According to the TOF values of the HGR-N_2H_4 at Au@Rh core–shell nanodendrites with and without light irradiation, we calculate that the contribution of light irradiation at identical reaction temperatures is approximately 47% ((16.8–8.9)/16.8 = 0.47). To explore the effect of the structure on the catalytic activity, a mixture of Au nanoparticles and Rh nanodendrites was synthesized (Supplementary Figure S13). Experimental results show that light irradiation does not affect the catalytic performance of the mixture for the HGR-N_2H_4 (Supplementary Figure S14), which in turn indicates that the close contact between the Au cores and Rh shells is critical for the electron transfer from the Au atoms to Rh atoms under light irradiation conditions.

In addition to the activity, the durability of catalyst is also a crucial factor for practical applications. The catalytic performance of bimetallic Au@Rh core–shell nanodendrites for the HGR-N_2H_4 is still maintained even after seven cycles (Figure 4d). TEM images show that the morphology of bimetallic Au@Rh core–shell nanodendrites is maintained without changes after seven cycles (Supplementary Figure S15). The particular branched structure of metal nanodendrites effectively inhibits the Ostwald ripening/aggregation phenomenon,[59] which is responsible for the excellent durability of bimetallic Au@Rh core–shell nanodendrites.

CONCLUSIONS

In summary, we have developed a facile one-pot strategy for the synthesis of bimetallic Au@Rh core–shell nanodendrites with LSPR property and controllable shell thickness. The preferential reduction of $HAuCl_4$ resulted in the formation of Au nanocrystals in the initial stage that then acted as the cores for the growth of Rh shells.

During the synthesis, polyallylamine hydrochloride not only effectively served as a capping agent to inhibit the aggregation of nanocrystals but also acted as a linker agent to promote the deposition of Rh on the Au cores. The as-prepared bimetallic Au@Rh core–shell nanodendrites exhibited significantly improved catalytic activity for the HGR-N_2H_4 compared with commercial Rh nanocrystals due to the atomically ultrathin structure of the 2D Rh nanoplates. Meanwhile, the as-prepared bimetallic Au@Rh core–shell nanodendrites displayed unusual light-enhanced catalytic activity for the HGR-N_2H_4 due to the LSPR property of the Au cores. Unfortunately, the as-prepared bimetallic Au@Rh core–shell nanodendrites exhibited low H_2 selectivity for the HGR-N_2H_4 (Supplementary Figure S16); this may be solved in our future work by the synthesis of RhNi alloy shells.

CONFLICT OF INTEREST

The authors declare no conflict of interest.

ACKNOWLEDGEMENTS

This work was supported by the 111 Project (B14041), the National Natural Science Foundation of China (grant number 21473111) and the Fundamental Research Funds for the Central Universities (grant numbers GK201602002, GK201701007 and GK201703029).

1 Zhang, L., Xie, Z. X. & Gong, J. L. Shape-controlled synthesis of Au-Pd bimetallic nanocrystals for catalytic applications. *Chem. Soc. Rev.* **45**, 3916–3934 (2016).
2 Gawande, M. B., Goswami, A., Asefa, T., Guo, H. Z., Biradar, A. V., Peng, D. L., Zboril, R. & Varma, R. S. Core-shell nanoparticles: synthesis and applications in catalysis and electrocatalysis. *Chem. Soc. Rev.* **44**, 7540–7590 (2015).
3 Liu, H. I., Nosheen, F. & Wang, X. Noble metal alloy complex nanostructures: controllable synthesis and their electrochemical property. *Chem. Soc. Rev.* **44**, 3056–3078 (2015).
4 Lim, B., Jiang, M., Camargo, P. H. C., Cho, E. C., Tao, J., Lu, X., Zhu, Y. & Xia, Y. Pd-Pt bimetallic nanodendrites with high activity for oxygen reduction. *Science* **324**, 1302–1305 (2009).
5 Zhou, Y., Wang, D. & Li, Y. Pd and Au@Pd nanodendrites: a one-pot synthesis and their superior catalytic properties. *Chem. Commun.* **50**, 6141–6144 (2014).
6 Tee, S. Y., Ye, E., Pan, P. H., Lee, C. J., Hui, H. K., Zhang, S. Y., Koh, L. D., Dong, Z. & Han, M. Y. Fabrication of bimetallic Cu/Au nanotubes and their sensitive, selective, reproducible and reusable electrochemical sensing of glucose. *Nanoscale* **7**, 11190–11198 (2015).
7 Wang, L., Dong, Y., Zhang, Y., Zhang, Z., Chi, K., Yuan, H., Zhao, A., Ren, J., Xiao, F. & Wang, S. PtAu alloy nanoflowers on 3D porous ionic liquid functionalized graphene-wrapped activated carbon fiber as a flexible microelectrode for near-cell detection of cancer. *NPG Asia Mater.* **8**, e337 (2016).
8 Yang, T., Ling, H., Lamonier, J. F., Jaroniec, M., Huang, J., Monteiro, M. J. & Liu, J. A synthetic strategy for carbon nanospheres impregnated with highly monodispersed metal nanoparticles. *NPG Asia Mater.* **8**, e240 (2016).
9 Jung, N., Bhattacharjee, S., Gautam, S., Park, H. Y., Ryu, J., Chung, Y. H., Lee, S. Y., Jang, I., Jang, J. H., Park, S. H., Chung, D. Y., Sung, Y. E., Chae, K. H., Waghmare, U. V., Lee, S. C. & Yoo, S. J. Organic-inorganic hybrid PtCo nanoparticle with high electrocatalytic activity and durability for oxygen reduction. *NPG Asia Mater.* **8**, e237 (2016).
10 Ye, E. Y., Regulacio, M. D., Zhang, S. Y., Loh, X. J. & Han, M. Y. Anisotropically branched metal nanostructures. *Chem. Soc. Rev.* **44**, 6001–6017 (2015).
11 Niu, Z., Becknell, N., Yu, Y., Kim, D., Chen, C., Kornienko, N., Somorjai, G. A. & Yang, P. Anisotropic phase segregation and migration of Pt in nanocrystals en route to nanoframe catalysts. *Nat. Mater.* **15**, 1188–1194 (2016).
12 You, H. J., Yang, S. C., Ding, B. J. & Yang, H. Synthesis of colloidal metal and metal alloy nanoparticles for electrochemical energy applications. *Chem. Soc. Rev.* **42**, 2880–2904 (2013).
13 Gu, J., Zhang, Y. W. & Tao, F. Shape control of bimetallic nanocatalysts through well-designed colloidal chemistry approaches. *Chem. Soc. Rev.* **41**, 8050–8065 (2012).
14 Wu, B., Liu, D., Mubeen, S., Chuong, T. T., Moskovits, M. & Stucky, G. D. Anisotropic growth of TiO_2 onto gold nanorods for plasmon-enhanced hydrogen production from water reduction. *J. Am. Chem. Soc.* **138**, 1114–1117 (2016).
15 Linic, S., Aslam, U., Boerigter, C. & Morabito, M. Photochemical transformations on plasmonic metal nanoparticles. *Nat. Mater.* **14**, 567–576 (2015).
16 Rej, S., Hsia, C. F., Chen, T. Y., Lin, F. C., Huang, J. S. & Huang, M. H. Facet-dependent and light-assisted efficient hydrogen evolution from ammonia borane using gold-palladium core-shell nanocatalysts. *Angew. Chem. Int. Ed.* **55**, 7222–7226 (2016).
17 Zheng, Z. K., Tachikawa, T. & Majima, T. Plasmon-enhanced formic acid dehydrogenation using anisotropic Pd-Au nanorods studied at the single-particle level. *J. Am. Chem. Soc.* **137**, 948–957 (2015).
18 Essinger-Hileman, E. R., DeCicco, D., Bondi, J. F. & Schaak, R. E. Aqueous room-temperature synthesis of Au-Rh, Au-Pt, Pt-Rh, and Pd-Rh alloy nanoparticles: fully tunable compositions within the miscibility gaps. *J. Mater. Chem.* **21**, 11599–11604 (2011).
19 Jiao, J., Liu, X. & He, H. Au@Rh core–shell nanoparticles with dendritic structure. *Mater. Lett.* **131**, 336–339 (2014).
20 Fan, Z. X., Huang, X., Tan, C. L. & Zhang, H. Thin metal nanostructures: synthesis, properties and applications. *Chem. Sci.* **6**, 95–111 (2015).
21 An, B. Z., Li, M. J., Wang, J. L. & Li, C. X. Shape/size controlling syntheses, properties and applications of two-dimensional noble metal nanocrystals. *Front. Chem. Sci. Eng.* **10**, 360–382 (2016).
22 Zhao, L., Xu, C., Su, H., Liang, J., Lin, S., Gu, L., Wang, X., Chen, M. & Zheng, N. Single-crystalline rhodium nanosheets with atomic thickness. *Adv. Sci.* **2**, 201500100 (2015).
23 Duan, H., Yan, N., Yu, R., Chang, C. R., Zhou, G., Hu, H. S., Rong, H., Niu, Z., Mao, J., Asakura, H., Tanaka, T., Dyson, P. J., Li, J. & Li, Y. Ultrathin rhodium nanosheets. *Nat. Commun.* **5**, 3093 (2014).
24 Pi, Y. C., Zhang, N., Guo, S. J., Guo, J. & Huang, X. Q. Ultrathin laminar Ir superstructure as highly efficient oxygen evolution electrocatalyst in broad pH range. *Nano Lett.* **16**, 4424–4430 (2016).
25 Saleem, F., Xu, B., Ni, B., Liu, H., Nosheen, F., Li, H. & Wang, X. Atomically thick Pt-Cu nanosheets: self-assembled sandwich and nanoring-like structures. *Adv. Mater.* **27**, 2013–2018 (2015).
26 Sun, Y., Gao, S., Lei, F., Liu, J., Liang, L. & Xie, Y. Atomically-thin non-layered cobalt oxide porous sheets for highly efficient oxygen-evolving electrocatalysts. *Chem. Sci.* **5**, 3976–3982 (2014).
27 Singh, S. K., Zhang, X. B. & Xu, Q. Room-temperature hydrogen generation from hydrous hydrazine for chemical hydrogen storage. *J. Am. Chem. Soc.* **131**, 9894–9895 (2009).
28 Yu, N. F., Tian, N., Zhou, Z. Y., Huang, L., Xiao, J., Wen, Y. H. & Sun, S. G. Electrochemical synthesis of tetrahexahedral rhodium nanocrystals with extraordinarily high surface energy and high electrocatalytic activity. *Angew. Chem. Int. Ed.* **53**, 5097–5101 (2014).
29 Jiang, Y., Su, J., Yang, Y., Jia, Y., Chen, Q., Xie, Z. & Zheng, L. A facile surfactant-free synthesis of Rh flower-like nanostructures constructed from ultrathin nanosheets and their enhanced catalytic properties. *Nano Res.* **9**, 849–856 (2016).
30 Sneed, B. T., Kuo, C. H., Brodsky, C. N. & Tsung, C. K. Iodide-mediated control of rhodium epitaxial growth on well-defined noble metal nanocrystals: synthesis, characterization, and structure-dependent catalytic properties. *J. Am. Chem. Soc.* **134**, 18417–18426 (2012).
31 Bai, J., Xu, G. R., Xing, S. H., Zeng, J. H., Jiang, J. X. & Chen, Y. Hydrothermal synthesis and catalytic application of ultrathin rhodium nanosheet nanoassemblies. *ACS Appl. Mater. Interfaces* **8**, 33635–33641 (2016).
32 Zheng, Z., Tachikawa, T. & Majima, T. Single-particle study of Pt-modified Au nanorods for plasmon-enhanced hydrogen generation in visible to near-infrared region. *J. Am. Chem. Soc.* **136**, 6870–6873 (2014).
33 Garcia, S., Anderson, R. M., Celio, H., Dahal, N., Dolocan, A., Zhou, J. & Humphrey, S. M. Microwave synthesis of Au-Rh core-shell nanoparticles and implications of the shell thickness in hydrogenation catalysis. *Chem. Commun.* **49**, 4241–42413 (2013).
34 Chantry, R. L., Siriwatcharapiboon, W., Horswell, S. L., Logsdail, A. J., Johnston, R. L. & Li, Z. Y. Overgrowth of rhodium on gold nanorods. *J. Phys. Chem. C* **116**, 10312–10317 (2012).
35 Kittel, C. *Introduction to Solid State Physics* 8th edn John Wiley & Sons: Hoboken, New Jersey, USA, (2008).
36 Wen, Y. N. & Zhang, J. M. Surface energy calculation of the fcc metals by using the MAEAM. *Solid State Commun.* **144**, 163–167 (2007).
37 Mazumder, V. & Sun, S. Oleylamine-mediated synthesis of Pd nanoparticles for catalytic formic acid oxidation. *J. Am. Chem. Soc.* **131**, 4588–4589 (2009).
38 Zhao, P., Cao, N., Su, J., Luo, W. & Cheng, G. NiIr nanoparticles immobilized on the pores of MIL-101 as highly efficient catalyst toward hydrogen generation from hydrous hydrazine. *ACS Sustainable Chem. Eng.* **3**, 1086–1093 (2015).
39 Wang, N., Sun, Q., Bai, R., Li, X., Guo, G. & Yu, J. In situ confinement of ultrasmall Pd clusters within nanosized silicalite-1 zeolite for highly efficient catalysis of hydrogen generation. *J. Am. Chem. Soc.* **138**, 7484–7487 (2016).
40 Zhu, Q. L., Tsumori, N. & Xu, Q. Immobilizing extremely catalytically active palladium nanoparticles to carbon nanospheres: a weakly-capping growth approach. *J. Am. Chem. Soc.* **137**, 11743–11748 (2015).
41 Burris, S. C., Zhou, Y., Maupin, W. A., Ebelhar, A. J. & Daugherty, M. W. The effect of surface preparation on apparent surface pK(a)'s of omega-mercaptocarboxylic acid self-assembled monolayers on polycrystalline gold. *J. Phys. Chem. C* **112**, 6811–6815 (2008).
42 Gilroy, K. D., Ruditskiy, A., Peng, H. C., Qin, D. & Xia, Y. Bimetallic nanocrystals: syntheses, properties, and applications. *Chem. Rev.* **116**, 10414–10472 (2016).
43 Seh, Z. W., Liu, S., Low, M., Zhang, S. Y., Liu, Z., Mlayah, A. & Han, M. Y. Janus Au-TiO_2 photocatalysts with strong localization of plasmonic near-fields for efficient visible-light hydrogen generation. *Adv. Mater.* **24**, 2310–2314 (2012).
44 Loganathan, B., Chandraboss, V. L., Senthilvelan, S. & Karthikeyan, B. Surface enhanced vibrational spectroscopy and first-principles study of l-cysteine adsorption on noble trimetallic Au/Pt@Rh clusters. *Phys. Chem. Chem. Phys.* **17**, 21268–21277 (2015).

45 Jang, K., Kim, H. J. & Son, S. U. Low-temperature synthesis of ultrathin rhodium nanoplates via molecular orbital symmetry interaction between rhodium precursors. *Chem. Mater.* **22**, 1273–1275 (2010).
46 Takata, T., Pan, C., Nakabayashi, M., Shibata, N. & Domen, K. Fabrication of a core-shell-type photocatalyst via photodeposition of group IV and V transition metal oxyhydroxides: an effective surface modification method for overall water splitting. *J. Am. Chem. Soc.* **137**, 9627–9634 (2015).
47 Singh, S. K., Singh, A. K., Aranishi, K. & Xu, Q. Noble-metal-free bimetallic nanoparticle-catalyzed selective hydrogen generation from hydrous hydrazine for chemical hydrogen storage. *J. Am. Chem. Soc.* **133**, 19638–19641 (2011).
48 Singh, S. K. & Xu, Q. Complete conversion of hydrous hydrazine to hydrogen at room temperature for chemical hydrogen storage. *J. Am. Chem. Soc.* **131**, 18032–18033 (2009).
49 Singh, A. K., Yadav, M., Aranishi, K. & Xu, Q. Temperature-induced selectivity enhancement in hydrogen generation from Rh-Ni nanoparticle-catalyzed decomposition of hydrous hydrazine. *Int. J. Hydrogen Energy* **37**, 18915–18919 (2012).
50 Zhang, Z. P., Zhu, W., Yan, C. H. & Zhang, Y. W. Selective synthesis of rhodium-based nanoframe catalysts by chemical etching of 3d metals. *Chem. Commun.* **51**, 3997–4000 (2015).
51 Li, C., Wang, T., Chu, W., Wu, P. & Tong, D. G. Synthesis of octahedral, truncated octahedral, and cubic Rh2Ni nanocrystals and their structure-activity relationship for the decomposition of hydrazine in aqueous solution to hydrogen. *Nanoscale* **8**, 7043–7055 (2016).
52 Saleem, F., Zhang, Z., Xu, B., Xu, X., He, P. & Wang, X. Ultrathin Pt-Cu nanosheets and nanocones. *J. Am. Chem. Soc.* **135**, 18304–18307 (2013).
53 Cheong, W. C., Liu, C., Jiang, M., Duan, H., Wang, D., Chen, C. & Li, Y. Free-standing palladium-nickel alloy wavy nanosheets. *Nano Res.* **9**, 1–7 (2016).
54 Tee, S. Y., Win, K. Y., Teo, W. S., Koh, L. D., Liu, S., Teng, C. P. & Han, M. Y. Recent progress in energy-driven water splitting. *Adv. Sci.* **4**, 1600337 (2017).
55 Sarina, S., Zhu, H., Jaatinen, E., Xiao, Q., Liu, H., Jia, J., Chen, C. & Zhao, J. Enhancing catalytic performance of palladium in gold and palladium alloy nanoparticles for organic synthesis reactions through visible light irradiation at ambient temperatures. *J. Am. Chem. Soc.* **135**, 5793–5801 (2013).
56 Singh, S. K. & Xu, Q. Nanocatalysts for hydrogen generation from hydrazine. *Catal. Sci. Technol.* **3**, 1889–1900 (2013).
57 He, L., Liang, B., Li, L., Yang, X., Huang, Y., Wang, A., Wang, X. & Zhang, T. Cerium-oxide-modified nickel as a non-noble metal catalyst for selective decomposition of hydrous hydrazine to hydrogen. *ACS Catal.* **5**, 1623–1628 (2015).
58 Tong, D. G., Chu, W., Wu, P., Gu, G. F. & Zhang, L. Mesoporous multiwalled carbon nanotubes as supports for monodispersed iron-boron catalysts: improved hydrogen generation from hydrous hydrazine decomposition. *J. Mater. Chem. A* **1**, 358–366 (2013).
59 Wang, L. & Yamauchi, Y. Metallic nanocages: synthesis of bimetallic Pt–Pd hollow nanoparticles with dendritic shells by selective chemical etching. *J. Am. Chem. Soc.* **135**, 16762–16765 (2013).

Supplementary Information accompanies the paper on the NPG Asia Materials website (http://www.nature.com/am)